Density, construction, and drag coefficient of electrostatic volcanic ash aggregates

M. R. James, S. J. Lane, and J. S. Gilbert

Department of Environmental Science, Institute of Environmental and Natural Sciences, Lancaster University, Lancaster, UK

Received 5 June 2002; revised 6 May 2003; accepted 14 May 2003; published 17 September 2003.

[1] Recent laboratory experiments have demonstrated that electrostatic charges generated during the fragmentation of volcanic pumice cause rapid aggregation of the silicate particles produced. Here, we present measurements of the mass and component particle size distribution of individual, electrostatically bound aggregates produced during these experiments. Particles produced by fracturing pumice aggregated as they fell ~1.5 m within an enclosed fall chamber. Aggregate mass measurements indicate aggregate densities of ~200 kg m^{-3} or less. The component particle size analysis demonstrates exponential-type cumulative distributions which are dominated (on a volume basis) by particles ~10–40 μm in diameter and contain few particles >70 μm. By representing these particles as disks of 5 μm thickness the calculated aggregate densities are in agreement with those derived from the aggregate mass measurements and indicate a relatively constant aggregate density with size (in contrast with previous results from fall velocities). Combining the density measurements with fall velocity data allows the drag coefficient of aggregates to be determined. Empirical equations developed to describe the particle size distribution within aggregates are used to derive relative aggregation coefficients for the electrostatic aggregation process. Our results can be used within numerical models of volcanic plumes in order to improve their representation of electrostatic aggregation processes. *INDEX TERMS:* 8404 Volcanology: Ash deposits; 8409 Volcanology: Atmospheric effects (0370); 8499 Volcanology: General or miscellaneous; *KEYWORDS:* electrostatic ash aggregate, drag coefficient, density

Citation: James, M. R., S. J. Lane, and J. S. Gilbert, Density, construction, and drag coefficient of electrostatic volcanic ash aggregates, *J. Geophys. Res.*, *108*(B9), 2435, doi:10.1029/2002JB002011, 2003.

1. Introduction

[2] The aggregation of small silicate particles (<100 μm in diameter) within volcanic plumes is a process that is known to occur, but which is currently poorly understood. Some aggregates (accretionary lapilli), which form in humid plumes, can develop significant mechanical strength due to cementation by minerals precipitating from evaporating liquid layers [*Gilbert and Lane*, 1994; *Sparks et al.*, 1997]. This greatly enhances their preservation potential, allowing them to be observed within deposits. Hence the internal composition, shape and density of accretionary lapilli can be studied with relative ease [*Schumacher and Schmincke*, 1991].

[3] In contrast, "dry" aggregates, which are bound mainly by electrostatic forces, are extremely delicate. Once on the ground, moisture, in combination with contact with Earth, allows charges to be neutralized. Thus intimate contact with other particles and aggregates determine that original aggregate structures usually have a maximum lifetime of hours to days. Therefore, although they may be much more common than accretionary lapilli, the only evidence for dry aggregate deposition is generally their collective influence on the deposit thickness and grain-size distribution. Some dry aggregates have been collected as they fell from eruption plumes [*Booth and Walker*, 1973; *Sorem*, 1982; *Sparks et al.*, 1997], but their individual component particle size distributions have not previously been analyzed. For several documented eruptions, this type of loosely bound, dry aggregate has been interpreted as being responsible for the secondary thickening of ashfall deposits and their bimodal grain size distributions [*Carey and Sigurdsson*, 1982; *Brazier et al.*, 1983; *Cornell et al.*, 1983; *Wiesner et al.*, 1995]. Significant differences between deposit parameters and the results of numerical models which exclude aggregation (notably the early deposition of particles sufficiently small that they would be expected to be transported far from the volcano) indicate that sedimentation of dry, electrostatic aggregates can be extremely important [*Carey and Sigurdsson*, 1982; *Cornell et al.*, 1983]. This importance is emphasized by the fact that the silicate particles which are the most affected by the aggregation process (generally those <100 μm in size) represent >70 wt % of some deposits [*Cornell et al.*, 1983].The implications of poor understanding of the aggregation process and the nature of aggregates therefore range from the miscalculation of eruption parameters from ashfall

0148-0227/03/2002JB002011$09.00

deposits to significant errors in predicted ash hazards for future eruptions.

[4] Previously, estimates of aggregate sizes and densities have been obtained by adjusting the parameters of numerical plume models in order for the results to fit the parameters of known deposits [*Carey and Sigurdsson*, 1982; *Brazier et al.*, 1983; *Cornell et al.*, 1983; *Wiesner et al.*, 1995]. This approach has indicated aggregate densities between 1200 and 200 kg m^{-3} and "average" aggregate sizes of 200 to ~500 μm. The results of laboratory fall velocity experiments [*James et al.*, 2002] have supported these values and further suggested that smaller aggregates (<200 μm) had higher densities (up to ~600 kg m^{-3}) than larger ones (>200 μm, 100 to 200 kg m^{-3}). However, in order to calculate these values, aggregate drag coefficients had to be assumed to be those of falling spheres [*James et al.*, 2002], dictating that the density values obtained were "equivalent" densities, representing a combination of the real aggregate density and any shape or structure factors which may also affect fall velocity.

[5] The bulk size distribution of particles incorporated into aggregates has also been previously estimated from deposits, where the fine mode of bimodal particle size distributions is interpreted to represent the small, aggregated particles which fell simultaneously with larger, individual particles [*Carey and Sigurdsson*, 1982; *Cornell et al.*, 1983; *Brazier et al.*, 1983]. Associated numerical models have aggregated all particles <63 μm [*Carey and Sigurdsson*, 1982], or 25% of particles 22 to 31 μm, 75% of particles 16 to 22 μm and all particles <16 μm [*Cornell et al.*, 1983] or particles between 15 and 125 μm [*Wiesner et al.*, 1995] in order to best fit the observations. Bimodal deposits have also been observed within laboratory experiments [*Schumacher*, 1994; *James et al.*, 2002], but the interpretation that these are formed by simultaneous deposition of aggregates and particles has not been independently verified by direct assessment of the component particle size distributions of individual aggregates.

[6] In this paper, we build on recent experimental work concerning the physical characteristics of electrostatic aggregates [*James et al.*, 2002] by further constraining the density of laboratory generated dry aggregates and determining their component particle size distributions. Using these data we develop empirical relations which allow the total mass and component particle size distribution for an aggregate of given size to be determined. Combining these with a distribution which describes the range of aggregate sizes produced allows relative aggregation coefficients to be calculated. Finally, with the value for aggregate density measured in this work, the aggregate fall velocity results of *James et al.* [2002] are used in order to obtain aggregate drag coefficients. The results will be of use for incorporating electrostatic aggregation processes into plume models as has recently been carried out for accretionary lapilli [*Veitch and Woods*, 2001].

[7] In keeping with the approach of *James et al.* [2002], throughout this paper we use the equations for spheres to relate aggregate sizes, masses and densities. Aggregate size is given by the "equivalent aggregate diameter", d_a, which is the diameter of a circle equivalent in area to a 1:1 image of the aggregate. Consequently, aggregate mass is given by $\pi d_a^3 \rho/6$, where ρ is the aggregate density. Because of its simplicity, this equivalent sphere representation is useful for modeling the properties of electrostatic aggregates. However, it should not be taken to imply real, physical densities or porosities because aggregate shapes have been shown to be highly irregular [*James et al.*, 2002].

2. Aggregate Density and Component Particle Size Distributions

[8] In order to measure the density and component particle size distributions of individual aggregates, laboratory experiments were carried out to produce aggregates from particles generated by fracturing pumice. Individually collected aggregates were either weighed (in order to calculate their density) or their component particles were dispersed for particle size analysis. For all the experiments described here, the pumice used was from the 18 May 1980 Mount St. Helens fall deposit.

2.1. Experimental Method

[9] Aggregates were produced with the apparatus described by *James et al.* [2002], which consists of a particle production unit located at the top of a draught-proof chamber. Particles were generated by repeatedly colliding two centimeter-sized pumice samples together using a solenoid at 2 Hz, producing ~0.2 mg of particles per impact. The particles became electrostatically charged during this pumice fracturing process [*James et al.*, 1998; *James*, 1999; *James et al.*, 2000] as a result of fracto-emission [*Donaldson et al.*, 1988], and this drove the aggregation as they fell (~1.5 m) within the chamber. Thus charge was not artificially introduced and was generated by the process believed responsible for the electrification of volcanic plumes [*James et al.*, 2000]. The mass loading within the columns of falling particles is calculated to be between $\sim 10^{-2}$ and 10^{-5} kg m^{-3} [*James et al.*, 2002], which is within estimates for the density of neutrally buoyant volcanic plumes ($<10^{-2}$ kg m^{-3}) [*Sparks et al.*, 1997]. Although the size of the largest particles produced (~1 mm) was limited by the relatively low impact energies (impact velocities were ~0.7 m s^{-1}), this brittle fracture process is thought to be representative of the dominant small particle generation mechanism within explosive eruptions. The particles produced were similar in size and shape to those observed in fine grained ashfall deposits [*James*, 1999; *James et al.*, 2002].

[10] In order to collect aggregates for mass measurements and density calculations, preweighed, glass coverslips were placed on glass collection strips at the base of the apparatus. Particles and aggregates landing on the coverslips were gently removed with a fine brush, to leave only one aggregate on each coverslip. Each aggregate was digitally imaged through an optical microscope for size analysis before the coverslips were reweighed. A Cahn Electrobalance with a resolution of ±1 μg up to a maximum mass of 250 mg (each coverslip was ~110 mg) was used for the weighing. Despite the microgram resolution, repeatability problems (which were probably the result of electrostatic charge) indicated a more limited accuracy for the mass measurements and suggested that a cautious error of ±10 μg should be used. Because of the low density (and therefore small mass) of the aggregates investigated, this error pre-

vented any useful mass measurements of aggregates less than ~400 μm in diameter.

[11] In order to carry out component particle size analysis of individual aggregates, another experiment was carried out without coverslips on the glass collection strips. After all of the particulate material had settled, each collection strip was individually extracted and the majority of the deposit on it removed, to leave approximately 10 aggregates untouched. The area around each was then cleaned further under magnification to ensure that no individual particles remained and digital images were taken of the aggregates.

[12] Each aggregate was then dispersed by putting a drop of filtered, deionized water onto it with a syringe and allowing it to evaporate. For the smallest aggregates investigated with this technique (~50 μm), this was a delicate procedure but, when carried out successfully, produced well dispersed particles. For significantly larger aggregates (>300 μm), the procedure was relatively simple but did not always reliably disperse the particles sufficiently for analysis. Attempts to increase the dispersion by using dilute solutions (to remove electrostatic attraction between the particles) and soaps (to reduce surface tension effects) proved fruitless due to residues left by the evaporating liquids which obscured particles. For the largest aggregates investigated (~850 to 1100 μm), where a satisfactory dispersion of the finest particles could not be achieved, the analysis was therefore limited to measuring the largest particle incorporated into each aggregate. Under the microscope, due to their morphology and three-dimensional form, these large particles were easily distinguished from non-dispersed clumps of smaller ones.

[13] After the water had evaporated, the area covered by each dispersed aggregate was then digitally imaged through a microscope. Larger aggregates required >300 images in order to cover the entire dispersal area, and the smallest aggregates required ~30. The image processing and analysis used for these images was the same as employed on the images of whole aggregates. Images were first thresholded then binarized in Micrografx Picture Publisher before being analyzed for particle size using Scion Image. The data obtained represent the area (in pixels) covered by each particle or aggregate. These values were converted into real areas (μm^2) and then represented by the diameters of equivalent area circles (the "equivalent diameter") for interpretation and presentation.

[14] The digital imaging was carried out with a Pixera camera mounted on a transmitted light microscope and, when imaging the entire area of a dispersed aggregate with multiple images, a linear stage was used to ensure and facilitate complete spatial coverage. Optical resolution was not an issue when imaging complete aggregates but limited the size of the smallest particles which could be detected within the dispersions. From theory, the size of the smallest features which can be resolved by a light microscope (assuming that their separation is equal to or greater than their size) is given as half the distance of the Rayleigh criterion, Δx [*Vollrath*, 1999], where

$$\Delta x = 0.61 \frac{\lambda}{NA}, \quad (1)$$

λ is the wavelength used and NA is the numerical aperture of the objective lens. For most of the particle sizing, an objective with NA = 0.12 was used and, taking λ to be 0.55 μm, this gives a Rayleigh resolution of 1.4 μm. With this microscope configuration, the digital image pixel size was ~0.73 × 0.73 μm. Dispersed particles from the two smallest aggregates were imaged using an objective with NA = 0.24, giving a Rayleigh resolution of 0.7 μm and, with this lens, the pixel size was ~0.30 × 0.30 μm. Thus, for both lenses used, the digital images were capable of producing data representing sizes smaller than could have been effectively resolved by the Rayleigh-limited optics. Data in this category were a result of noise during the digitization, errors in the thresholding or possibly diffraction effects. Therefore, during analysis, subresolution sized "particles" were excluded from the particle size distributions, but their count has been used to give an estimate of the maximum error in the total particle counts.

2.2. Results

[15] The densities of 32 aggregates, as calculated from their measured masses and assuming an equivalent spherical shape, are shown in Figure 1a. Despite the relative magnitude of the errors, the data clearly suggest aggregate densities of <300 kg m^{-3}. Several different trends can be interpreted in the data. If the entire data set is considered as one, then a gradually decreasing density with increasing diameter would be appropriate. However, images of the landed aggregates suggest that the larger aggregates may have spread out somewhat during impact (Figure 2), effectively increasing their measured diameter and thus decreasing their calculated densities. This is illustrated by landed aggregates larger than ~700 μm typically demonstrating little internal structure, relatively circular shapes and being surrounded by halos of broken off particles (e.g., the uppermost image in Figure 2). Smaller aggregates generally appear more coherent, with highly irregular shapes, observable internal structures and few, if any, separated particles. Therefore, for examining the density data, aggregates smaller or larger than ~700 μm could be considered separately and, in this case, a constant density may be applicable to each group, with averages of ~200 ± 25 kg m^{-3} for small aggregates and ~83 ± 5 kg m^{-3} for larger aggregates. If this density difference is entirely due to the artifact of larger aggregates spreading out during landing, it would imply that their equivalent diameters have been overestimated by up to ~35%. This is believed to be an entirely plausible value, implying that the measured decrease in aggregate densities with increasing diameter could be a result only of the overestimation of diameters.

[16] In order to help further constrain aggregate densities, values have also been estimated from the particle size analyses. Thirteen of the aggregates collected for particle size analysis were successfully dispersed and, given the known size of each particle within an aggregate, the total solid mass can be calculated if an average particle shape and density (2200 kg m^{-3}) are assumed. Combining this with the measured size of the aggregate (calculated from its equivalent diameter and assuming a spherical shape) allows an estimate of the aggregate density to be made. Figure 1b gives the results of these calculations carried out assuming either a spherical or a flat disk (5 μm thick) shape for the individual component particles. Considering that most of the component particles are shards of bubble walls [*James*,

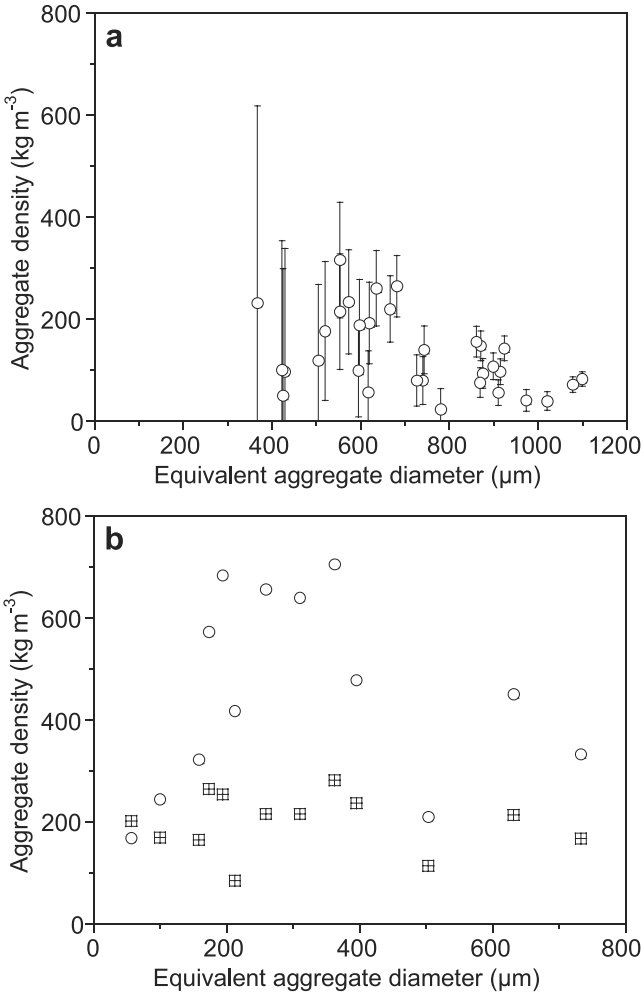

Figure 1. Aggregate densities. (a) Densities calculated from mass measurements of individual aggregates versus equivalent aggregate diameter (the diameter of a circle of equivalent area to that of the image of the landed aggregate). The significant errors (representing ±10 μg in the mass measurement) reflect the small magnitude of the masses involved and the probable influence of electrostatic forces on the balance. (b) Aggregate densities calculated from the component particle size data of 13 aggregates. Open circles give the resulting aggregate densities if the component particles are represented as spheres, and crossed squares give the results if the component particles are represented by 5 μm thick disks.

1999], the spherical particle model is expected to overestimate the density considerably, and the results are shown in Figure 1b for reference. The disk particle model is thought most likely to closely represent the real situation, particularly for the smaller aggregates (<700 μm) and has been shown to represent particle surface areas in some rhyolitic ash deposits considerably better than spheres [*Riley et al.*, 2003].

[17] The disk model produces density values which demonstrate an independence from aggregate size. However, their average value is sensitive to the particle thickness chosen. SEM images of particles produced by the apparatus [*James*, 1999] suggest that a disk thickness <10 μm would be appropriate. Using a value of 5 μm gives 200 kg m^{-3} (Figure 1b), but thicknesses of 4 or 6 μm give 160 and 240 kg m^{-3}, respectively. Therefore we use these data only to determine the independence of aggregate density from aggregate size (for aggregates smaller than ~750 μm), and assign a density value (200 kg m^{-3}) on the basis of the mass measurements (Figure 1a) of aggregates believed to be unaffected by spreading during landing (those <700 μm in diameter). Thus, in the rest of the paper, a constant aggregate density of 200 kg m^{-3} is used.

[18] The component particle size data from individual aggregates allowed the total number of constituent particles

Figure 2. Images of collapsed aggregates. Ten images, representative of the range of sizes and morphologies observed (scale bar is 500 μm). The aggregates were imaged on glass plates using transmitted light. The uppermost aggregate demonstrates the typical collapse morphology of large aggregates (>700 μm), with no discernable internal structure, a generally circular outline, and a surrounding halo of broken off particles. This can be compared with the smaller aggregates (<700 μm), which show much less evidence of collapse and spreading on impact and demonstrate considerable internal porosity, irregular outlines and few detached particles.

larger than 1.4 μm in each aggregate to be counted and the results are given in Figure 3a, plotted against the equivalent aggregate diameter. For simplicity, the data have been fitted with two power laws although a more complex curve would be more likely to reflect the underlying growth mechanism. For aggregates larger than ~150 μm, the number of component particles increases with a near cubic relation, as would be expected if the component particle size distribution and aggregate density remained constant. Under these conditions, the number of component particles is directly proportional to the aggregate volume which, for a spherical representation, increases with d_a^3. However, at diameters less than ~150 μm a different slope may be appropriate (giving $d_a^{1.6}$). Although only two data points fall away from the trend for larger aggregates these points represent the totals of 171 and 389 individual component particle counts and we therefore have confidence in their values. Given that aggregate densities appear to be approximately constant (Figure 1b), the slope of 1.6 (Figure 3a) must represent a significant change in the particle size distribution within these aggregates, with larger aggregates containing some increasingly larger component particles.

[19] This is supported by Figure 3b, which gives the component particle size distributions for the analyzed aggregates. The data are presented as cumulative distributions where, at any diameter, the value represents the number of particles of that size or larger and, on the log linear axes, many of the distributions give straight lines or shallow curves. The steeper slopes for the smaller aggregates indicate distributions more dominated by smaller particles than those of the larger (>150 μm) aggregates. By (noncumulative) volume, the distributions' modes occur over a range of diameters from ~7 to 33 μm (if component particles are represented as spheres) or from ~5 to 17 μm (if component particles are represented as disks).

[20] In Figure 3b only particle size data <70 μm have been plotted in order to demonstrate the major trends. However, most of the aggregates also contain small proportions of considerably larger particles. These coarser particles comprise only a small fraction (generally <2%)

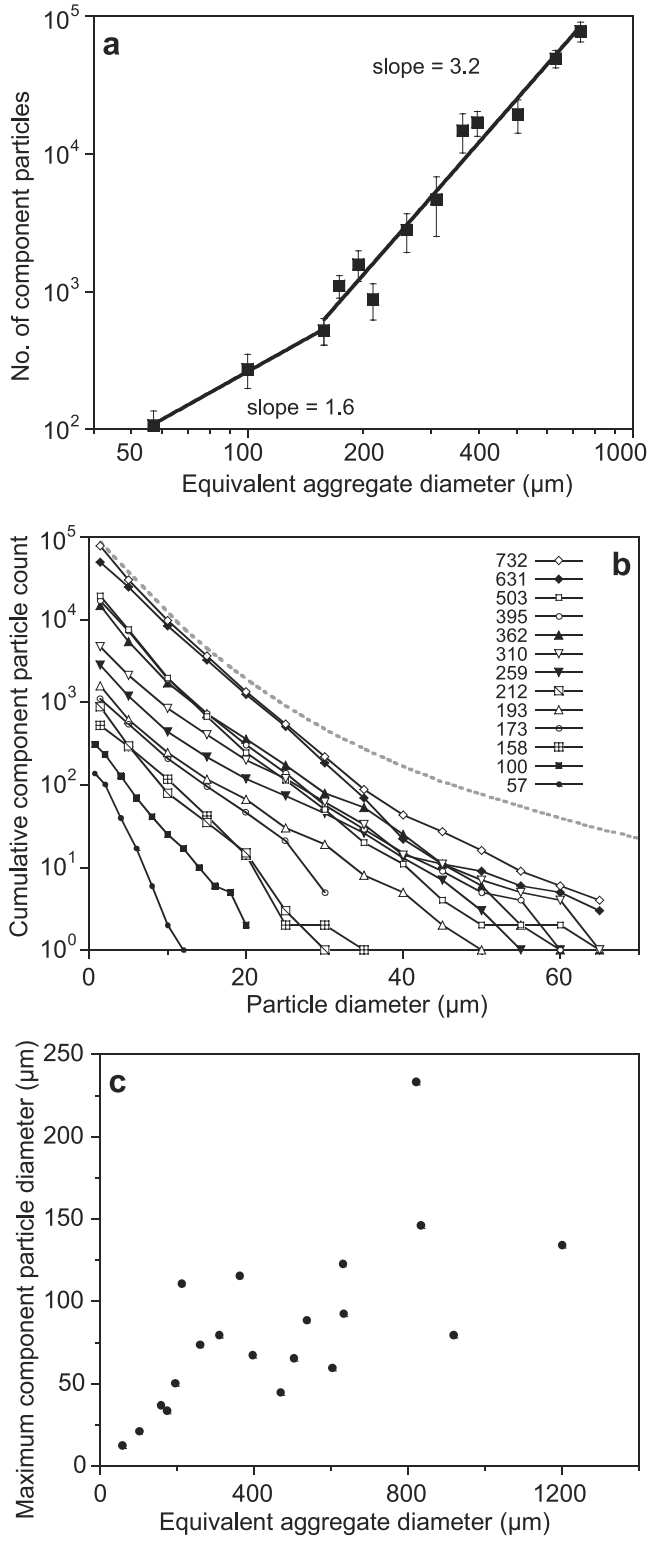

Figure 3. (opposite) Particles contained within aggregates. (a) Total number of component particles larger than 1.4 μm in individual aggregates. For aggregates with equivalent diameters >150 μm, the number of component particles follows a near cubic relation, supporting a constant density sphere representation for the aggregates. Although only two significantly smaller aggregates were investigated, they suggest a shallower slope for aggregates <150 μm in equivalent diameter. In order to illustrate the sensitivity of the data to the number of the smallest particles, error bars have been plotted representing the total number of apparent particles counted in each aggregate which have calculated diameters smaller than the theoretical resolution of the microscope optics (see text). (b) Cumulative component particle size distributions for these aggregates, with each line representing the distribution from one aggregate. The grey dashed line represents the relative size distribution describing all the particles produced by the apparatus (see section 4). Particle counts at any point represent the number of component particles of that or larger diameter. The aggregate equivalent diameters are given in the key (in microns). For clarity, only data <70 μm have been plotted; however, most of the aggregates showed small numbers of significantly larger component particles, the maximum diameters of which are given in Figure 3c. Figure 3c also contains data from aggregates which were only sufficiently dispersed for analysis of the largest component particle but not for a complete particle size distribution.

of the total volume, and the largest particle observed within individual aggregates are shown in Figure 3c. The data suggest that aggregates smaller than ~200 μm have a maximum particle size which is a relatively strong function of the aggregate size. The majority of larger aggregates appear to have maximum particle sizes between 50 and 150 μm and demonstrate a much weaker relationship with aggregate diameter and increased scatter.

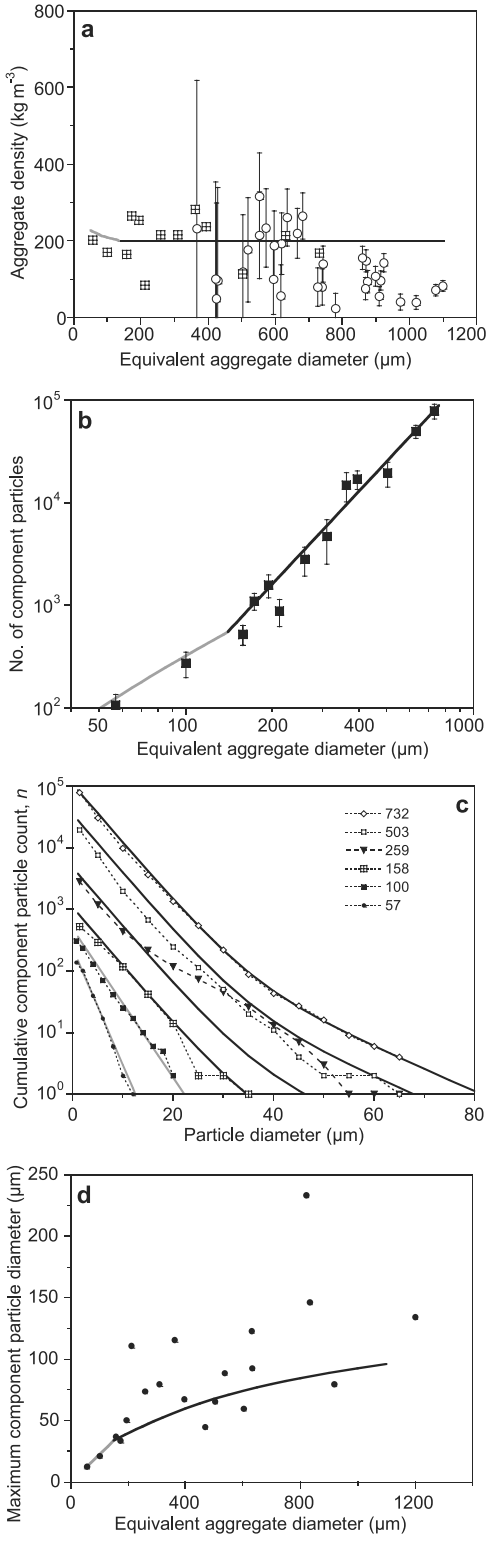

2.3. Aggregation Model

[21] In order to estimate the total particle size distribution within a collection of aggregates, empirical relations to describe the size distribution of component particles of individual aggregates (i.e., Figure 3b) have been derived (Figure 4). The presence of relatively straight lines and straight line segments in Figure 3b suggests that exponential-type distributions are suitable. Therefore we represent the cumulative component particle size distribution within any aggregate of given size (≥140 μm in equivalent diameter) by the sum of two exponential distributions multiplied by a scaling factor to reflect the total number of component particles;

$$n = 0.000272 d_a^{\,3}\left[\exp(-0.22 d_p) + 0.008\exp(-0.083 d_p)\right], \quad d_a \geq 140\mu m, \tag{2}$$

where n is the number of particles larger than a diameter d_p within an aggregate of equivalent diameter d_a (Figure 3b). The coefficients were determined by comparing model results to the measured aggregate densities (using the 2200 kg m^{-3}, 5-μm-thick disk component particle model), particle size distributions and total particle numbers given in the previous section. Note that our data constrain this relation only for aggregates smaller than ~850 μm and, as shown in Figure 4c, the model fits the data from some aggregates better than it does for others, reflecting the natural variability within the aggregates. In Figure 4d, equation (2) is shown to produce a reasonable value for the maximum component particle diameter (by setting n = 1) within aggregates.

[22] However, equation (2) was found to fit the data for aggregates smaller than 140 μm poorly (and produced invalid results such as component particles larger than the host aggregate). Thus a second relation is given for aggregates smaller than 140 μm (Figure 4c);

$$n = 1.2 d_a^{1.3}\exp\left(-10.9 d_p d_a^{-0.797}\right), \qquad d_a < 140\ \mu m. \tag{3}$$

In this case, the limited data are fitted best by a component particle size distribution which varies with the size of the aggregate; hence d_a is included within the exponential

Figure 4. (opposite) Model representation of aggregate data. In all plots, the solid lines represent the model results (equation (2) in black, equation (3) in grey). (a) Aggregate densities. The circles give the densities calculated from the aggregate mass measurements (Figure 1a) and the crossed squares represent the densities calculated from the measured component particle size distributions (Figure 1b) with a 5-μm-thick disk particle model. (b) Total component particle numbers (for particles >1.4 μm), as obtained from the component particle size analyses. (c) Cumulative component particle size distributions for six of the analyzed aggregates whose equivalent diameters (in microns) are given in the key. (d) Predicted maximum particle size in an aggregate (i.e., n = 1 in equations (2) and (3)) compared with the measured data.

function in equation (3). The density values calculated by equation (3) increase slightly with decreasing aggregate diameter (Figure 4a); however, given the magnitude of scatter within experimental data, this is not deemed to be significant. Note that the power of d_a in equations (2) and (3) (3 and 1.3, respectively) defines the slope of the total number of component particles results (Figure 4b) and are close to the values obtained from the best line fits to the data (3.2 and 1.6 in Figure 3a).

3. Aggregation Coefficients

[23] The aggregation coefficient [*Gilbert and Lane*, 1994] of a particle of a certain size represents its probability of being incorporated into an aggregate and is thus a product of both particle collision and sticking coefficients. From experiments carried out in a recirculating wind tunnel, *Gilbert and Lane* [1994] calculated relative aggregation coefficients for particles incorporated into accretionary lapilli. Although it is not possible to calculate coefficients directly from our experiments (due to aggregates never being completely separable from individual particles in complete deposits), an estimate can be made by combining the model results for component particle sizes (equations (2) and (3)) with an aggregate size distribution. This provides the estimated total size distribution of all aggregated particles, which can then be compared with particle size data for a deposit as a whole (containing particles which fell incorporated into aggregates and those that fell individually).

[24] From experimental data on particles aggregating during ~1 m of fall, *James et al.* [2002] gives the cumulative aggregate size distribution produced as

$$n_a \propto \exp(-0.01 d_a), \tag{4}$$

where n_a is the number of aggregates larger than a diameter d_a (in microns). Using this to determine the relative number of aggregates of any particular diameter, the total component particle size distribution of all aggregated particles (Figure 5a) can be obtained from equations (2) and (3).

[25] Also shown in Figure 5a are two cumulative particle size distributions obtained from deposits produced within our apparatus (by an Elzone particle sizer [*Karuhn and Berg*, 1984]), which have been scaled to coincide with the model results at a particle diameter of 10 μm (i.e., so that all data sets have the same number of particles larger than 10 μm). The Elzone data acquired using a 300 μm orifice tube (which allowed particles down to 10 μm to be analyzed) suggest that particles >10 μm have a decreasing probability of being incorporated into aggregates with increasing size. In order to analyze smaller particles, a 120 μm orifice tube was used and the coincidence of these data with the model results suggest that particles between ~4 and 10 μm in size have an approximately constant likelihood of being incorporated into aggregates. The use of the 120 μm tube required that the sample was sieved at 70 μm and this, combined with inherent difficulties in merging data sets taken with different orifice tubes, is the reason for the variation between the overlapping section of the Elzone data sets.

[26] For particle sizes >10 μm, ratioing the 300 μm orifice tube Elzone data with the model gives an aggregation coefficient which, due to the scaling described above, is defined as being relative to a coefficient of 1 at 10 μm. This relative aggregation coefficient is plotted in Figure 5b along with the equivalent coefficient determined by *Gilbert and Lane* [1994] for accretionary lapilli. For particle sizes between 4 and 10 μm, the coincidence of the Elzone data with the model results (Figure 5a) implies that these particle sizes also have an aggregation coefficient of 1. Figure 5b

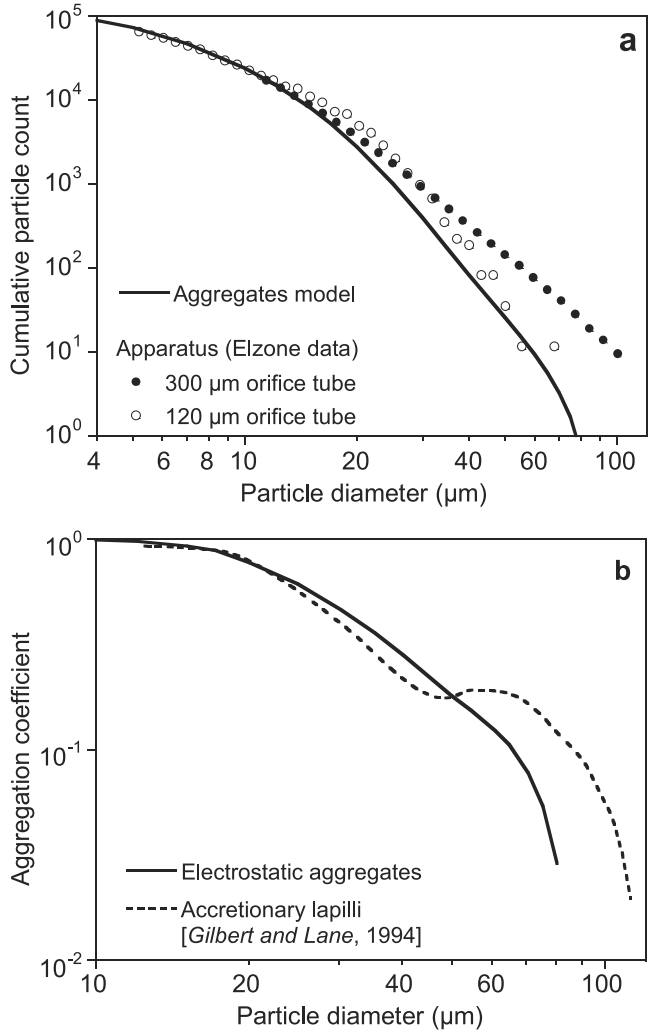

Figure 5. Aggregation coefficients. (a) Total cumulative particle size distribution (solid line) for particles incorporated into a distribution of aggregates, as determined from equations (2) to (4). The symbols represent Elzone particle size data from the particulate material produced by the apparatus (i.e., all particles, whether or not they have been incorporated into aggregates), which have been scaled to coincide with the model results at 10 μm. The solid symbols give data obtained with a 300 μm orifice tube, using particles which were sieved at 250 μm and the open symbols give data obtained with a 120 μm orifice tube, after sieving at 70 μm. (b) A relative aggregation coefficient, derived from ratioing the model results and the 300 μm data set for particles >10 μm, and the aggregation coefficient determined by *Gilbert and Lane* [1994] for accretionary lapilli.

demonstrates that while dry aggregation may be slightly more efficient at accumulating particles between ~20 and 50 μm in size, in the presence of a liquid phase, accretionary lapilli can scavenge much larger ones.

4. Drag Coefficients

[27] The drag coefficient, C_d, of a body moving at a velocity, v, in a fluid is defined by

$$C_d = \frac{F_d}{\frac{1}{2}\rho_f v^2 A}, \quad (5)$$

where F_d is the drag force, ρ_f is the density of the fluid (1.23 kg m^{-3} for sea level atmosphere), and A is the projected area of the body onto a plane perpendicular to the direction of motion [*Batchelor*, 1967]. For an object falling at its terminal velocity, then $F_d = mg$, where m is its mass and g is the acceleration due to gravity, giving

$$C_d = \frac{mg}{\frac{1}{2}\rho_f v^2 A}. \quad (6)$$

Therefore, if an aggregate is represented as a sphere of measured size and fall velocity, and the density value given in section 2.2 (200 kg m^{-3}) is used to calculate its mass, then its drag coefficient can be determined from equation (6).

[28] Here we examine the data of *James et al.* [2002], who produced aggregates using the apparatus described in this paper and measured fall velocities directly by imaging strobe-illuminated aggregates [*James et al.*, 2002, Figure 5] as they fell. Aggregate sizes were determined as the diameter of a circle of equivalent area to the illuminated side view of each aggregate and aggregate drag coefficients have been calculated as described above by representing the aggregates as spheres with a density of 200 kg m^{-3}. The results are given by the open symbols in Figure 6a, plotted against the aggregates' Reynolds number, $Re = v\rho_f d_a/\mu$, where μ is the fluid viscosity (1.7×10^{-5} Pa s for sea level atmosphere). The large degree of scatter in the data is probably mainly due to the simple spherical representation of the irregular aggregate shapes.

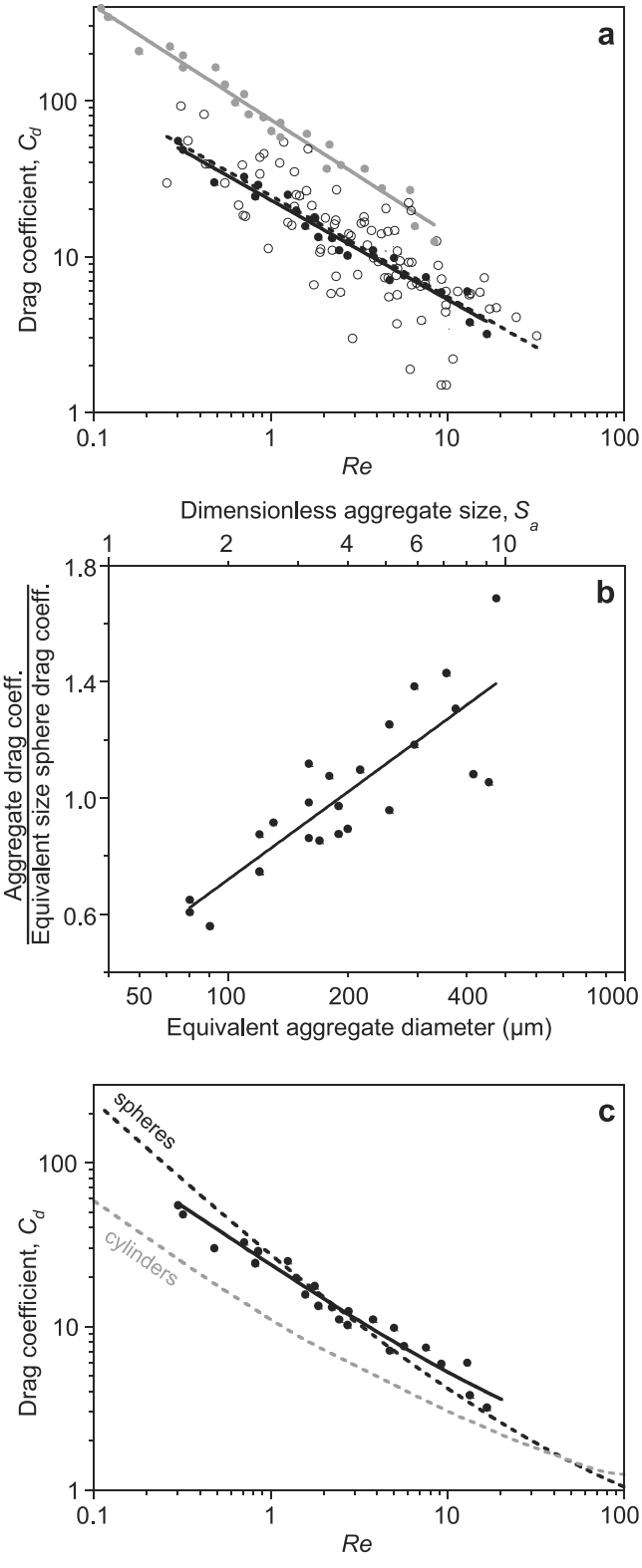

Figure 6. (opposite) Aggregate drag coefficients. (a) Drag coefficients for the aggregates investigated by *James et al.* [2002] plotted against Reynolds number. Open symbols represent measurements from individual falling aggregates, and their best fit power law is given by the dashed line. Solid symbols give the drag coefficients calculated from aggregate distributions (where velocity equivalence is assumed with single falling particles modeled as spheres [*James et al.*, 2002]), and grey symbols represent results from the same data but recalculated for velocity equivalence with single particles modeled using the *Wilson and Huang* [1979] drag curve (see text). Best fit power laws are given by the appropriate shade solid lines. Given the coincidence in the results from individual measurements with those from aggregate distributions using the sphere model, only this latter data set is used in Figures 6b and 6c. (b) Ratio of aggregate drag coefficients to those of equivalently sized spheres versus aggregate diameter, with the dimensionless aggregate size parameter, S_a, (equation (9)) given on the top axis. (c) Aggregate drag coefficients compared with drag curves for spheres and infinite cylinders [*Hoerner*, 1965]. Solid black curve representing the results of equation (10), which defines aggregate drag coefficients using the drag curve for spheres and the aggregate size parameter, S_a.

[29] In a second type of experiment, *James et al.* [2002] horizontally separated falling particles and aggregates within a slow crosswind as a function of their fall velocities. The material landed on glass collection strips (oriented orthogonal to the crosswind direction) and the fall velocity of aggregates on any one strip was assumed to approximate to that of individual particles which had landed on the same strip. This effectively allowed fall velocities to be ascribed to collections of aggregates, therefore decreasing scatter in the data. Aggregate and coincident individual particle sizes were determined by optical methods similar to those described here (section 2.1) and representative diameters were obtained for 25 different aggregate distributions. The aggregate diameters were then assigned fall velocities equal to those calculated for the coincident single particles and here, we have derived aggregate drag coefficients using these velocities. However, this dictates that our aggregate drag coefficient values depend on the velocity model used to calculate the fall velocity of the individual particles.

[30] In Figure 6a, the solid black symbols represent the calculated aggregate drag coefficients where velocity equivalence was assumed with individual falling particles whose fall velocities were determined from the standard drag curve for spheres [*Clift et al.*, 1978]. The power law best fit line for these results (solid black line) can be seen to be nearly coincident with that from the individual aggregates (dashed black line). However, it has been shown that representing volcanic particles as spheres can significantly overestimate their fall velocity, particularly for shard-like particles [*Riley et al.*, 2003; *Wilson and Huang*, 1979]. Therefore aggregate drag coefficients have also been determined assuming velocity equivalence with the particles where particle fall velocities have been calculated from the Re-C_d relation for individual falling particles

$$C_{d(particle)} = \frac{24}{Re}F^{-0.828} + 2\sqrt{1.07 - F}, \quad (7)$$

given by *Wilson and Huang* [1979] (for $\sim 0.1 < Re < 100$). F is a particle shape factor which is 1 for a sphere and decreases with decreasing sphericity. Here, we use a value of $F = 0.3$ which best fits the fall velocity data of *Riley et al.* [2003] for rhyolitic ash shards. The recalculated aggregate drag coefficient results are given in Figure 6a by the grey symbols and plot significantly above the other data.

[31] Therefore the aggregate drag coefficient values calculated for the individual measurements (open symbols, Figure 6a) follow the trend of the smallest values of the range believed to be possible from the horizontal separation experiments. Although the individual measurements do not rely on a fall velocity model (velocity was measured directly), they do require estimates for aggregate mass and an aerodynamic cross-sectional area (A), both of which are calculated from the equivalent diameter as determined from the imaged area of the side of each aggregate. In order to assess if this simplification could be responsible for significantly decreasing the calculated drag coefficient, the effect of changing the value of d_a was investigated. Simply altering d_a (thus changing both the calculated aggregate mass and aerodynamic area) would require that d_a is generally doubled in order for the individual measurements to coincide with the shard-like particle-equivalence dispersal results. Given that this is outside experimental errors for measurement of d_a and aggregate masses have been independently verified in this work, it has been discounted. Another possible source of error is the aerodynamic area (A) alone but, in this case, A would have had to have been overestimated by a factor of four, which is believed to be unlikely. Therefore the similarity between the results from individual measurements and the dispersal experiments where velocity equivalence was assumed with falling particles modeled as spheres is not thought to be coincidence and, given the lower degree of scatter in the latter data set, these results are used from now on.

[32] A power law best fit line to these data can be used to represent aggregate drag coefficients,

$$C_{d(agg)} = 23Re^{-0.637}; \quad (8)$$

however, the limited range (representing aggregate diameters between $\sim$50 and 500 μm) of the data dictates that this has been only demonstrated for $0.2 < Re < 20$ (Figure 6a). Because of the decreasing air density with height, experiments carried out at low pressures would be required in order for this trend to be extended to cover aggregates falling at altitude. A possible interim alternative would be to assume that the differences between the drag coefficients of aggregates and spheres are a simple function of aggregate size rather than involving the flow dynamics. This would suggest that, with respect to the flow dynamics, aggregates do fall as spheres and that differences between the drag coefficients are mainly due to errors in calculation of the aggregates' equivalent diameters. In this case, aggregate drag coefficients can be formulated as a correction factor (a function of aggregate size alone) to the drag curve of a sphere. Here, the drag coefficients for spheres, $C_{d(\text{sphere})}$, have been calculated from experimental data given by *Clift et al.* [1978] (by using an empirical fit which had been derived previously in order to obtain fall velocity [*James et al.*, 2002]). In Figure 6b, the ratio of aggregate drag coefficient to that calculated for spheres of equivalent size and diameter is shown against aggregate diameter and a best line fit demonstrated. In order to nondimensionalize this, we introduce a dimensionless aggregate size factor S_a, where

$$S_a = \frac{d_a}{50}, \qquad 50 < d_a < 500\ \mu m, \quad (9)$$

and d_a is given in microns, allowing $C_{d(\text{agg})}$ to be given by

$$C_{d(\text{agg})} = C_{d(\text{sphere})} \times [0.42 + 0.43\ln(S_a)], \quad 1 < S_a < 10. \quad (10)$$

[33] This curve is plotted in Figure 6c to demonstrate its fit to the data and compare it to the drag curve for spheres. The drag curve for infinite cylinders perpendicular to their axes [*Hoerner*, 1965] is also shown because it has been previously found relevant to larger volcanic clasts [*Walker et al.*, 1971]. The aggregate data appear to lie parallel to this curve but cross the drag curve for spheres at $Re \approx 2.2$ (equivalent to aggregates of diameter $\sim$200 μm), with smaller aggregates having smaller and larger aggregates having larger drag coefficients than similarly sized spheres.

[34] The differences between the drag coefficients of aggregates and spheres could also be due to several other effects. The commonly used Re-C_d curves for spheres [*Hoerner*, 1965; *Clift et al.*, 1978] assume that they are impermeable, nonrotating and rigid; none of which can be assumed for aggregates. The images of landed aggregates demonstrate that they are mostly highly irregular in shape, with significantly sized internal pores. Air flow through a permeable aggregate would reduce the pressure differential across it, thus reducing drag, and this has been shown to be a substantial effect for fractal aggregates in water [*Johnson et al.*, 1996]. If this is the cause of our aggregate data falling off the drag curve for spheres (Figure 6c), then it would suggest that the effect of airflow through an aggregate is greater for smaller aggregates (they have smaller drag coefficients than similarly sized spheres). This is qualitatively supported by the constant aggregate porosity suggested by constant density, although, images of landed aggregates (Figure 2) do suggest that larger pores may exist in larger aggregates.

[35] Shape factors (most aggregates are far from spherical) will also change drag coefficients from those of spheres. Highly irregular shapes and rough surfaces are likely to increase drag and may also induce rotation or oscillation, which would further increase the drag coefficient. Although rapid rotations have not been observed [*James et al.*, 2002], as aerodynamic forces increase, aggregates may also change shape as they fall. In the case of raindrops, which change shape from spheres to a flatter morphology with increasing size and fall velocity, this increases drag coefficients for $Re > 300$ [*Pruppacher and Klett*, 1997].

5. Discussion

[36] Previously, it has been suggested that the growth of larger aggregates may be dominantly due to the collection of smaller aggregates, rather than from the continuous accretion of individual particles [*James et al.*, 2002]. Our images of collapsed aggregates (Figure 2) support this, demonstrating irregular shapes, fractal-like self-similarity and the presence of significant internal voids which are believed to represent the boundaries between accumulated aggregates. For aggregates larger than $\sim$700 μm, internal structures were generally not observed but we believe that this is due to their collapse on landing.

[37] We consider that the generation of the smallest, ''primary'' aggregates probably occurs rapidly after or during the production of the particles from the pumice fragmentation. The pumice fragmentation method generates particles both positively and negatively electrically charged, with high charge to mass ratios (specific charges) of up to 10^{-3} C kg^{-1} [*James et al.*, 2000]. During the collision of the pumice samples, the particles generated will be in intimate contact within small crush zones on the pumice surfaces and, immediately after the separation of the samples, the particles are at their highest number density within the air. Therefore, during these times, because for small, closely spaced, electrically charged particles, electrostatic forces can easily dominate those of gravity [*Blythe and Reddish*, 1979], interactions between the smallest particles are most abundant. Larger particles generally have significantly lower specific charges and are therefore more influenced by gravitational rather than electrostatic forces [*Blythe and Reddish*, 1979]. Thus the formation of an initial aggregate population is likely to be mainly the result of a high number of particle collisions due to small particle separation distances and relatively strong electrostatic forces. Some of the smaller aggregates observed (Figure 2) demonstrate a delicate and fingering form, similar to that of aggregates of latex spheres produced under microgravity, the formation of which is dominated by inertial and electrostatic forces [*Blum*, 2000].

[38] As aggregates grow they will accumulate particles with both positive and negative net charges. Consequently, the charge to mass ratio of a growing aggregate will rapidly decrease from that of an individual particle to that of all the particles as a whole (which can be a decrease of several orders of magnitude [*James et al.*, 2000]). Thus, with increasing aggregate size, electrostatic attraction will become decreasingly important for inducing collisions and fall velocity differences will become the dominant collision mechanism. However, electrostatic attraction is likely to retain its importance for particle binding because, when particles are in contact, attraction forces are dominated by the closest centers of charge (i.e., those on the neighboring particles) rather than that of the aggregate as a whole.

[39] Falling aggregates will collide with and accrete other aggregates and, as they grow, fall velocity differences between them and larger single particles will decrease. We believe that this eventually allows larger particles to be incorporated into aggregates rather than ''punching through'' or disaggregating them during collisions. We thus view the primary growth mechanism for electrostatic aggregates as a spectrum ranging from being dominated by electrostatic forces for the smallest aggregates, to being dominated by fall velocity differences at larger diameters. It is tempting to speculate that, within our apparatus, the changes in component particle size distributions for growing aggregates (Figures 3a and 3b) suggest that this transition in dominant aggregate growth mechanism occurs at around an aggregate size of $\sim$150 μm. It is possible that this is also reflected in aggregate size distributions and discontinuities in distributions at aggregate equivalent diameters of $\sim$150 and 50 μm were shown by *James et al.* [2002, Figure 3a], for experimental aggregates collected after 0.5 and 1.1 m of fall, respectively. Although these were initially interpreted as being probably due to the remaining presence of populations of small, individual, nonaggregated particles, we now believe that it is more likely that these populations comprised small aggregates whose growth had been dominated by electrostatic attraction, which had yet to be scavenged into larger aggregates.

[40] In this paper, we have used component particle size distributions and mass measurements of experimentally produced electrostatic aggregates to produce a model of the aggregate components and to analyze aggregate drag coefficients. However, a key difference between our experimental apparatus and the environment within a plume is the lack of recirculation and large-scale turbulence within the apparatus. Both of these phenomena may affect aggregation and disaggregation processes. During the experiments, turbulence was limited to that produced by the particle production apparatus and the falling particles themselves.

The effect of turbulence on aggregation mechanisms (studied for other applications and environments) is complex and varies with the fluid properties, the strength of the turbulence and the sizes of the aggregating material and aggregates produced [*Pruppacher and Klett*, 1997]. Although the presence of turbulence is likely to increase the probability of particles colliding [*Pruppacher and Klett*, 1997], it may also be directly responsible for breaking up large aggregates. For electrostatically charged silicate particles, the situation is further complicated by the unknown distribution of charges on individual particles which prevents any realistic estimate of the degree to which electrostatic forces will interact with other aggregation mechanisms. Within plumes, the turbulence strength varies with time and position and, depending on the intensity of particle and aggregate sedimentation, its influence on aggregation processes may be subsequently overprinted by interactions within the particulate material as it sediments through the atmosphere.

[41] Aggregation and disaggregation processes will occur simultaneously within plumes, with aggregate breakup being strongly controlled by aggregate strengths. Because of the insulating nature of the silicate particles and poor knowledge of the charge distributions involved, the magnitudes of the binding electrostatic forces within aggregates are difficult to estimate. However, it is possible that aggregate strength could be assessed from the collapse patterns of different sized aggregates, with images of aggregates larger than $\sim$700 μm suggesting that they land with an impact energy sufficient to break off some material and collapse (Figure 2), whereas, in general, smaller aggregates remain intact. Thus an estimate of the forces exerted during the landing of a $\sim$700 μm aggregate may represent the effective binding force within aggregates. If this force, F_l, is assumed to act constantly over the period during which an aggregate collapses completely onto a surface, t, then its magnitude can be estimated from the change in momentum

$$F_l t = m\Delta v, \tag{11}$$

where, for a 700 μm aggregate of density 200 kg m^{-3}, its mass, m, will be 3.6×10^{-8} kg and its fall velocity, v, will be 0.86 m s^{-1}. If the aggregate's velocity is assumed to decrease linearly during impact (from when the leading edge touches the surface to when the trailing edge lands), it will collapse during a time period, t, of 1.6 ms. This gives force of order 10^{-5} N which would represent an upper limit for the binding force of electrostatic aggregates. Note that from $F_l = ma$, where a is acceleration, this implies that aggregates can withstand accelerations of up to $\sim 50g$. This is undoubtedly an overestimate, but does suggest that aggregates may be more resilient within a turbulent environment than perhaps expected. It is also possible, if not highly likely, that aggregates can respond to aerodynamic forces by adjusting their shape, rather than breaking up.

[42] Despite the lack of turbulence within our experiments, their relevance to aggregation within volcanic plumes is supported by the similarities between our results and those of the limited previous field and numerical modeling work carried out on deposits. *James et al.* [2002] showed that measured fall velocities for laboratory aggregates coincided with those required by the numerical plume model of *Carey and Sigurdsson* [1982] in order to reconstruct the deposit produced by the 18 May 1980 Mount St. Helens eruption. The data presented here also allows the particle sizes involved to be considered. In order to reconstruct the particle size distribution due to aggregates within a deposit, the relative abundance of the different aggregate sizes must be known. However, equation (2) reflects that for aggregates >140 μm, the shape of the component particle size distribution (and thus the diameter at which it peaks, when given on a particle volume basis) does not appear to be a function of the aggregate diameter. Therefore any deposit dominated by aggregates larger than $\sim$140 μm in equivalent diameter will have the same volume maximum (in this case, at $\sim$14 μm if the particles are assumed to be spheres or $\sim$9 μm if they are represented as disks). This correlates well with the data of *Carey and Sigurdsson* [1982], who demonstrated a nearly constant fine mode (at 13 μm) in the bimodal fall deposit (up to 450 km from the volcano) produced by the 18 May 1980 Mount St. Helens eruption. Although our aggregate density results suggest that a value of 200 kg m^{-3} is applicable for aggregates up to at least $\sim$700 μm in equivalent diameter, for larger aggregates, a slightly lower value may be appropriate. However, we see no physical reason why aggregates should start to accumulate material in a less dense structure, which would be necessary for aggregate densities to decrease.

[43] The calculated aggregation coefficients demonstrate that, even without recirculation within our apparatus, a significant proportion of the smallest particles must be incorporated into aggregates. With a relative aggregation coefficient of $\sim$1 for all analyzed particles <10 μm (down to 4 μm) the effect of aggregation must be considered when assessing the deposition of these respirable particles for health hazards. This lack of diameter dependence for the aggregation coefficients of these particles suggests that their presence in aggregates is limited only by their abundance in the original particle size distribution. Given that the smallest aggregates, which are dominated by component particles in this size range, should be least susceptible to break up by turbulence, then we expect that in all plumes, a considerable fraction of these sized particles will be present as small aggregates. For particles smaller than $\sim$50 μm electrostatic aggregation coefficients have been shown to be similar to those previously calculated for accretionary lapilli [*Gilbert and Lane*, 1994]. However, accretionary lapilli are significantly more efficient at incorporating larger (i.e., 50 to several hundred microns) particles than electrostatic aggregates, which is to be expected given that surface tension, the dominant initial binding mechanism for accretionary lapilli [*Gilbert and Lane*, 1994; *Schumacher and Schmincke*, 1995], will provide much stronger binding forces for larger particles than could be available from electrostatic charges. To what degree the size of the largest incorporated particles (Figure 3c) within the experimental aggregates (which appears to tend to $\sim$100 μm) may have been determined by the total "starting" particle size distribution is difficult to assess. However, given that the calculated aggregation coefficients (Figure 5b) begin to decrease rapidly at component particle sizes of $\sim$70 μm, then we suspect that the maximum incorporated particle sizes were controlled

mainly by the aggregation process rather than the initial particle size distribution.

[44] Given that particle aggregation processes within plumes are still poorly understood, we believe that the presence of electrostatically bound aggregates should not be viewed as excluding the production of accretionary lapilli. This is supported by our own unpublished field observations of simultaneous sedimentation of both types of aggregate at Sakurajima volcano, Japan. Our experiments have demonstrated that electrostatic aggregates form extremely rapidly and it is entirely possible that subsequent accretionary lapilli growth could occur by the accumulation of previously produced electrostatic aggregates. Because of their delicate nature, any characteristic structures within electrostatic aggregates would not be expected to survive collision with an accretionary lapilli, thus evidence for the process may be difficult to detect. The same particle collision mechanisms are involved in both types of aggregation (although with different relative importance) and depend on fluid motion and the physical, electrical and aerodynamic properties of the particles and aggregates. Only after collision are surface tension forces relevant for particles covered with liquid layers and hence the particle binding efficiencies for dry and wet aggregates will be significantly different.

6. Conclusions

[45] The experiments have demonstrated that, despite their irregular shapes, aggregates can be represented as spheres with a density of $\sim$200 kg m^{-3} and a drag coefficient given by either equation (8) or (10). Size analysis of their component particles has shown exponential-type cumulative distributions and these have been represented by equations (2) and (3). Aggregation coefficients calculated using this model indicate that respirable particles <10 μm in diameter have a high and uniform probability of being incorporated into aggregates. Images of landed aggregates indicate that aggregates smaller than $\sim$140 μm are likely to be produced extremely rapidly and that larger aggregates grow dominantly by the accumulation of these smaller aggregates, but are also capable of incorporating significantly larger particles, possibly as their relative fall velocities decrease.

[46] **Acknowledgments.** This work was supported by The Leverhulme Trust (F/00 185A) and The Royal Society (574006.G503/19679). We are indebted to R. P. Hoblitt for supplying Mount St. Helens pumice and C. E. H. Windermere for use of their Elzone facility. Reviews by the associate editor, G. Ernst, C. Textor, and R. Peterson have significantly improved the text.

References

Batchelor, G. K., *An Introduction to Fluid Mechanics*, Cambridge Univ. Press, New York, 1967.

Blum, J., Laboratory experiments on preplanetary dust aggregation, *Space Sci. Rev.*, *92*, 265–278, 2000.

Blythe, A. R., and W. Reddish, Charges on powders and bulking effects, *Am. Inst. Phys. Conf. Ser.*, *48*, 107–114, 1979.

Booth, B., and G. P. L. Walker, Ash deposits from the new explosion crater, Etna 1971, *Philos. Trans. R. Soc. London, Ser. A*, *274*, 147–151, 1973.

Brazier, S., R. S. J. Sparks, S. N. Carey, H. Sigurdsson, and J. A. Westgate, Bimodal grain size distribution and secondary thickening in ash-fall ash layers, *Nature*, *301*, 115–119, 1983.

Carey, S. N., and H. Sigurdsson, Influence of particle aggregation on deposition of distal tephra from the May 18, 1980, eruption of Mount St. Helens volcano, *J. Geophys. Res.*, *87*, 7061–7072, 1982.

Clift, R., J. R. Grace, and M. E. Weber, *Bubbles, Drops and Particles*, Academic, San Diego, Calif., 1978.

Cornell, W., S. Carey, and H. Sigurdsson, Computer simulation of transport and deposition of the Campanian Y-5 ash, *J. Volcanol. Geotherm. Res.*, *17*, 89–109, 1983.

Donaldson, E. E., J. T. Dickinson, and S. K. Bhattacharya, Production and properties of ejecta released by the fracture of materials, *J. Adhesion*, *25*, 281–302, 1988.

Gilbert, J. S., and S. J. Lane, The origin of accretionary lapilli, *Bull. Volcanol.*, *56*, 398–411, 1994.

Hoerner, S. F., *Fluid-Dynamic Drag*, S. F. Hoerner, New York, 1965.

James, M. R., Electric charge within volcanic plumes on Earth and Io, Ph.D. thesis, Lancaster Univ., Lancaster, England, 1999.

James, M. R., S. J. Lane, and J. S. Gilbert, Volcanic plume monitoring using atmospheric electric potential gradients, *J. Geol. Soc. London*, *155*, 587–590, 1998.

James, M. R., S. J. Lane, and J. S. Gilbert, Volcanic plume electrification: Experimental investigation of a fracture charging mechanism, *J. Geophys. Res.*, *105*, 16,641–16,649, 2000.

James, M. R., J. S. Gilbert, and S. J. Lane, Experimental investigation of volcanic particle aggregation in the absence of a liquid phase, *J. Geophys. Res.*, *107*(B9), 2191, doi:10.1029/2001JB000950, 2002.

Johnson, C. P., X. Li, and B. Logan, Settling velocities of fractal aggregates, *Environ. Sci. Technol.*, *30*, 1911–1918, 1996.

Karuhn, R. F., and R. H. Berg, Practical aspects of Electrozone® size analysis, in *Particle Characterization in Technology*, vol. I, *Applications and Microanalysis*, edited by J. K. Beddow, CRC Press, Boca Raton, Fla., 1984.

Pruppacher, H. R., and J. D. Klett, *Microphysics of Clouds and Precipitation*, Kluwer Acad., Norwell, Mass., 1997.

Riley, C. M., W. I. Rose, and G. J. S. Bluth, Quantitative shape measurements of distal volcanic ash, *J. Geophys. Res.*, *108*, doi:10.1029/2001JB000818, in press, 2003.

Schumacher, R., A reappraisal of Mount St. Helens' ash clusters-depositional model from experimental observation, *J. Volcanol. Geotherm. Res.*, *59*, 243–260, 1994.

Schumacher, R., and H.-U. Schmincke, Internal structure and occurrence of accretionary lapilli-a case-study at Laacher See volcano, *Bull. Volcanol.*, *53*, 612–634, 1991.

Schumacher, R., and H.-U. Schmincke, Models for the origin of accretionary lapilli, *Bull. Volcanol.*, *56*, 626–639, 1995.

Sorem, R. K., Volcanic ash clusters: Tephra rafts and scavengers, *J. Volcanol. Geotherm. Res.*, *13*, 63–71, 1982.

Sparks, R. S. J., M. I. Bursik, S. N. Carey, J. S. Gilbert, L. S. Glaze, H. Sigurdsson, and A. W. Woods, *Volcanic Plumes*, John Wiley, Hoboken, N. J., 1997.

Veitch, G., and A. W. Woods, Particle aggregation in volcanic eruption columns, *J. Geophys. Res.*, *106*, 26,435–26,441, 2001.

Vollrath, W., Optical microscopy at sub-0.1 mm resolution: Fiction or vision?, in *Productronica 97*, *Proceedings HLF*, pp. 46–64, Fraunhofer IRB, Stuttgart, Germany, 1999.

Wiesner, M. G., Y. Wang, and L. Zheng, Fallout of volcanic ash to the deep South China Sea induced by the 1991 eruption of Mount Pinatubo (Philippines), *Geology*, *23*, 885–888, 1995.

Wilson, L., and T. C. Huang, The influence of shape on the atmospheric settling velocity of volcanic ash particles, *Earth Planet. Sci. Lett.*, *44*, 311–324, 1979.

Walker, G. P. L., L. Wilson, and E. L. G. Bowell, Explosive volcanic eruptions, I. The rate of fall of pyroclasts, *Geophys. J. R. Astron Soc.*, *22*, 377–383, 1971.

J. S. Gilbert, M. R. James, and S. J. Lane, Department of Environmental Science, Institute of Environmental and Natural Sciences, Lancaster University, Lancaster LA1 4YQ, UK. (j.s.gilbert@lancaster.ac.uk; m.james@lancaster.ac.uk; s.lane@lancaster.ac.uk)